High Lithium Storage Performance of FeS Nanodots in Porous Graphitic Carbon Nanowires

*Changbao Zhu, Yuren Wen, Peter A. van Aken, Joachim Maier, and Yan Yu**

Dedicated to Professor Rüdiger Kniep on the occasion of his 70th birthday

Much attention has been paid to increase the energy density of Li-ion batteries, in order to fulfill the requirements of electric vehicles and grid-scale energy storage. While for anodes various options are available, this is not at all the case for cathodes. In this context, the inexpensive and environmentally benign iron sulfides have been investigated as cathode materials due to the remarkably high capacity based on the conversion reaction. Here, the preparation of FeS nanodots accommodated in porous graphitic carbon nanowires is reported via a combination of electrospinning technique and biomolecular-assisted hydrothermal method. These materials exhibit excellent electrochemical performances also as cathode materials, with energy densities even higher than the current $LiCoO_2$ intercalation cathode. Moreover, key problems of conversion reaction, such as the low degree of reversibility, large polarization are far-reachingly mitigated.

1. Introduction

The energy density of conventional Li-ion batteries based on $LiMO_2$ (M = transition metal) cathodes and graphite anodes seems to have reached a practical upper limit due to the intense research and development efforts of last two decades.[1,2] In order to improve the energy density of Li-ion batteries, especially in view of the requirements of electric vehicles and grid-scale energy storage, transition metal compounds based on conversion reactions have attracted great attention.[3–5] Transition metal compounds, such as oxides,[6] sulfides,[7,8] fluorides[9] can offer substantially higher capacities than traditional intercalation compounds, by involving distinctly more than one electron per metal ion.[10,11] Among them, the inexpensive and environmentally benign iron sulfides[12–19] have been investigated as cathode materials owing to the high capacity of 609 mA h g^{-1} for FeS and 894 mA h g^{-1} for FeS_2 at reasonably high voltages, while the best $LiMO_2$ intercalation cathode can only provide capacities below 200 mA h g^{-1}.[20] In the late 20th century, molten salt FeS_2 (FeS)/Li–Al batteries for transportation application had been paid much attention to;[21] moreover, FeS_2 has been successfully commercialized as component of primary batteries with high energy density.[22] A rechargeable FeS_2(FeS)/Li battery, however, is still not commercially available. Besides the safety issues concerning lithium metal anodes, the conversion chemistry of iron sulfide cathode is a major challenge.[10] According to conversion reactions of iron sulfide (FeS_2 and FeS),[16,23,24] $FeS_2 + 4Li^+ + 4e^- \rightarrow Fe + 2Li_2S$ and $FeS + 2Li^+ + 2e^- \rightarrow Fe + Li_2S$, highly reactive nano-$Fe^0$ as well as highly resistive Li_2S will be formed through such a conversion reaction. As nano-Fe^0 agglomerate larger and isolated Li_2S and nonreactive α-Fe phase form, a rapid loss of capacity is observed.[25,26] Modification of pristine iron sulfide appears to be necessary to improve the reversibility of this conversion reaction.[27]

Compared to FeS_2, investigations of FeS are relatively scarce, and mostly performed to study its function as a potential anode (tested as 0–3 V vs Li^+/Li). The vast majority of these studies reported unsatisfying reversibility and rate performance.[28–30] Here we will demonstrate a remarkable performance as a consequence of optimizing the nanostructure. In spite of relatively low potential (≈1.6 V) of FeS compared with $LiCoO_2$, the at least four times higher capacity of FeS (FeS 609 mA h g^{-1} and $LiCoO_2$ 140 mA h g^{-1}) does lead to an even higher theoretical energy density when compared to $LiCoO_2$, which makes FeS attractive as cathode material, especially for room temperature rechargeable FeS/Li batteries with liquid electrolyte. Surprisingly (in view of the voltage) even the power output turns out to be remarkable. In addition, monosulphides, such as FeS are known to exhibit a relatively low voltage hysteresis compared with oxides and fluorides, which is beneficial for achieving a high energy efficiency.[27]

In order to arrive at rechargeable FeS/Li batteries, the typical issues related with conversion reactions need to be addressed first. As suggested by our previous work dealing

Dr. C. Zhu, Prof. J. Maier, Prof. Y. Yu
Max Planck Institute for Solid State Research
Heisenbergstr. 1, Stuttgart 70569, Germany
E-mail: yanyumse@ustc.edu.cn
Dr. Y. Wen, Prof. P. A. van Aken
Max Planck Institute for Intelligent Systems
Heisenbergstr. 3, Stuttgart 70569, Germany
Prof. Y. Yu
Key Laboratory of Materials for Energy Conversion
Chinese Academy of Sciences, Department of Materials Science and Engineering
University of Science and Technology of China
Hefei 230026, Anhui, P.R. China

DOI: 10.1002/adfm.201404468

with MoS_2, the inclusion of nanodots of the electroactive mass in carbon fibers leads to a powerful electrochemical integrated circuit in which the particles are mechanically decoupled but the electrochemically well connected, rendering a conversion reaction very reversible. The small dimensions of MoS_2 and the resulting reaction confinement gives, to a certain extent, rise to a "diffusion-less" and "nucleation-free" conversion.[31] Usually, the electrospun carbon nanofibers even if annealed at a high temperature (500–800 °C) will be amorphous and less active.[31–33] However, if highly porous graphitic carbon nanofibers or partial graphitic carbon nanofibers can be prepared, the rate performance of relevant materials is expected to be greatly improved.

Here, by combination of electrospinning technique and a biomolecular (L-cysteine)-assisted hydrothermal method, FeS nanodots (≈5–10 nm) dispersed in carbon nanowires (≈100 nm) are successfully prepared. Moreover, the fabricated carbon nanowires are advantageous compared with previous reported ones,[31,32] as we find them of graphitic nature and highly porous. They show a Brunauer-Emmett-Teller (BET) surface area of 226 $m^2 g^{-1}$ and a pore size distribution in the range of 1–10 nm. This morphology results in an excellent rate performance of FeS as regards Li storage. In spite of the expected complexity of the conversion reaction, indeed, well-defined, very flat and symmetric charge–discharge plateaus are observed, with a remarkably low total voltage loss in a cycle (less than 0.3 V) and a distinct reversibility.

2. Results and Discussions

Figure 1a illustrates the detailed preparation of such FeS nanodots accommodated in the porous graphitic carbon nanowires for which an electrospinning technique is combined with a biomolecular (L-cysteine)-assisted hydrothermal method. (We denote this nanostructure as nano-0D FeS ⊂ nano-1D porous graphitic carbon according to the notation of ref.[34] and abbreviated it further as FS-ND ⊂ PGC-NW in the following). For the electrospinning process, a viscous aqueous precursor solution containing $Fe(NO_3)_3$ and polyvinylpyrrolidone (PVP) is used. After annealing the as-prepared electrospun polymer nanofibers, Fe_3C/carbon nanowires form. Unlike the usual case that the polymer totally decomposes into amorphous carbon,[31–33] owing to the catalytic effect of Fe,[35] the amorphous carbon on the surface of Fe_3C turns into graphitic carbon, resulting in Fe_3C/graphitic carbon core-shell structures. Recently, biomolecular-assisted synthetic methods are considered as promising approaches for preparing nanosized materials, and L-cysteine has attracted great attention as a complexing, reducing agent, and simultaneously being a sulfur source.[36,37] (For

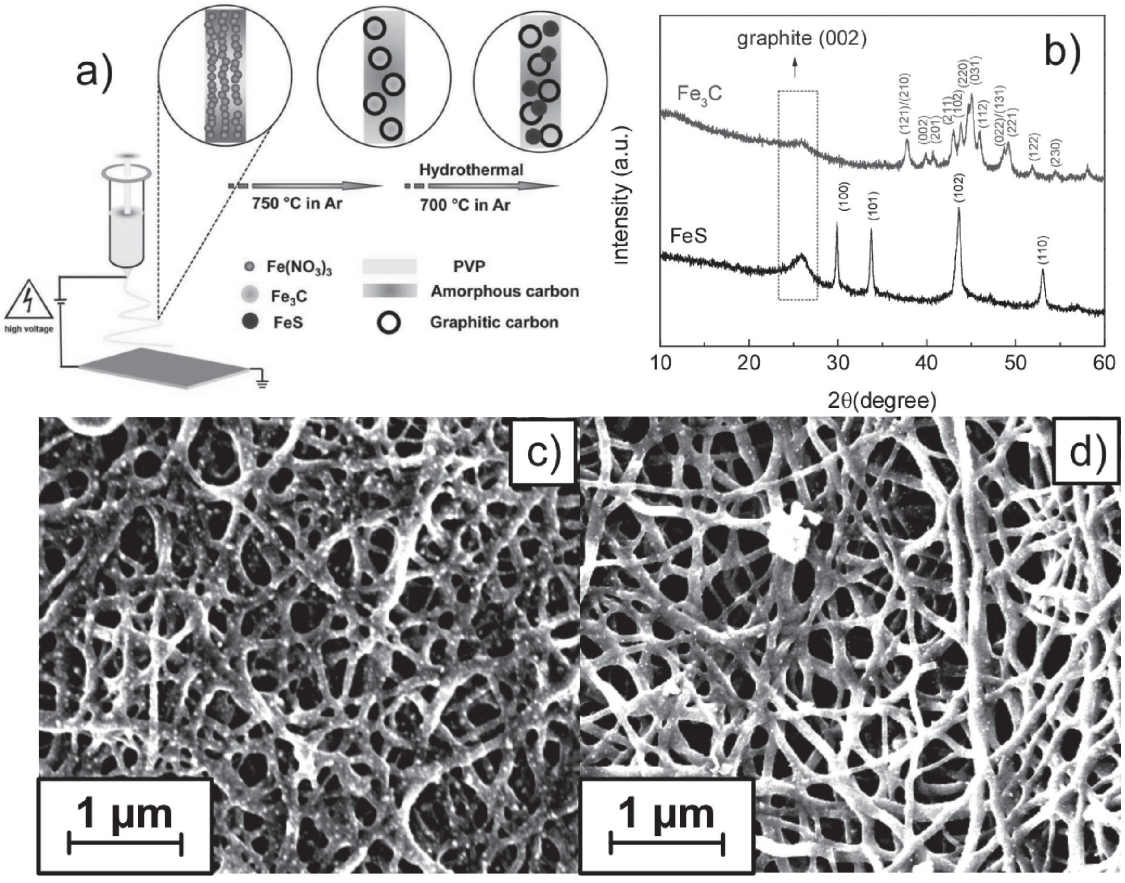

Figure 1. a) Schematic illustration of combination of electrospinning technique and biomolecular-assisted hydrothermal method to prepare FS-ND ⊂ PGC-NW. b) XRD patterns of intermediate product Fe_3C/carbon nanowire and final FS-ND ⊂ PGC-NW. c,d) SEM images of intermediate product Fe_3C/carbon nanowire and final FS-ND ⊂ PGC-NW, respectively.

the L-cysteine molecule, there are various functional groups, namely, $-NH_2$, –COOH, and –SH, which have a strong tendency to coordinate with inorganic cations and metals.)[38] For the fabrication of our FeS cathode, we apply such a L-cysteine-assisted hydrothermal method and combine it with a post heat treatment. During the hydrothermal process, the graphitic carbon shell of Fe_3C/C is cracked and Fe_3C diffuses out of the graphitic carbon shell. This promotes graphitization of the amorphous carbon, and results in the formation of pores. After the hydrothermal process and the post annealing, Fe_3C has totally transformed to FeS nanodots. The most likely reaction mechanism is as follows: The Iron ions, oxidatively freed from Fe_3C,[39] coordinate with L-cysteine to form initial precursor complexes. At the high reaction temperature (190 °C) of the hydrothermal process, the coordination bonds of the complexes break and iron sulfide forms.[38,39] After washed by water, the collected powder was further annealed at 700 °C, and finally FeS/C was obtained.

Figure 1b shows the X-ray diffraction (XRD) patterns of the Fe_3C/C and FeS/C nanowires. All the diffraction peaks can be indexed to Fe_3C (JCPDS 34–0001) and hexagonal FeS (JCPDS 65–9124) or graphitic carbon. The latter is detected in XRD patterns of both Fe_3C and FeS. The peak located at 26° corresponds to the (002) plane of graphite. As shown in scanning electron microscopy (SEM), both $Fe_3C \subset$ carbon nanowire and FeS ⊂ carbon nanowire are long, uniform, and continuous, and they are connected with each other to form a 3D network. The diameters of such nanowires are around 100 nm. In order to further investigate the microstructure of FS-ND ⊂ PGC-NW, transmission electron microscopy (TEM) and high-resolution TEM (HRTEM) were applied. As shown in **Figure 2**a, long and uniform nanowires with diameter of ≈100 nm are in good agreement with SEM images. In a larger magnification (Figure 2b), porous nanowires were observed. In most cases, pyrolytic carbon nanowires decomposed from polymer precursor (i.e., polyethyleneoxide (PEO), PVP, or polyacrylonitrile (PAN)) are found to be amorphous,[31–33] while here, the carbon nanowires are partially of graphitic nature. More precisely, as indicated in Figure 2c, amorphous carbon, graphitic carbon, and pores coexist inside the nanowires. The thickness of the graphitic carbon shells is around 5 nm. The interlayer distance of the graphitic carbon layers is 0.34 nm (Figure 2d), which corresponds to the (002) plane of graphite, in good agreement with XRD results (Figure 1b). The

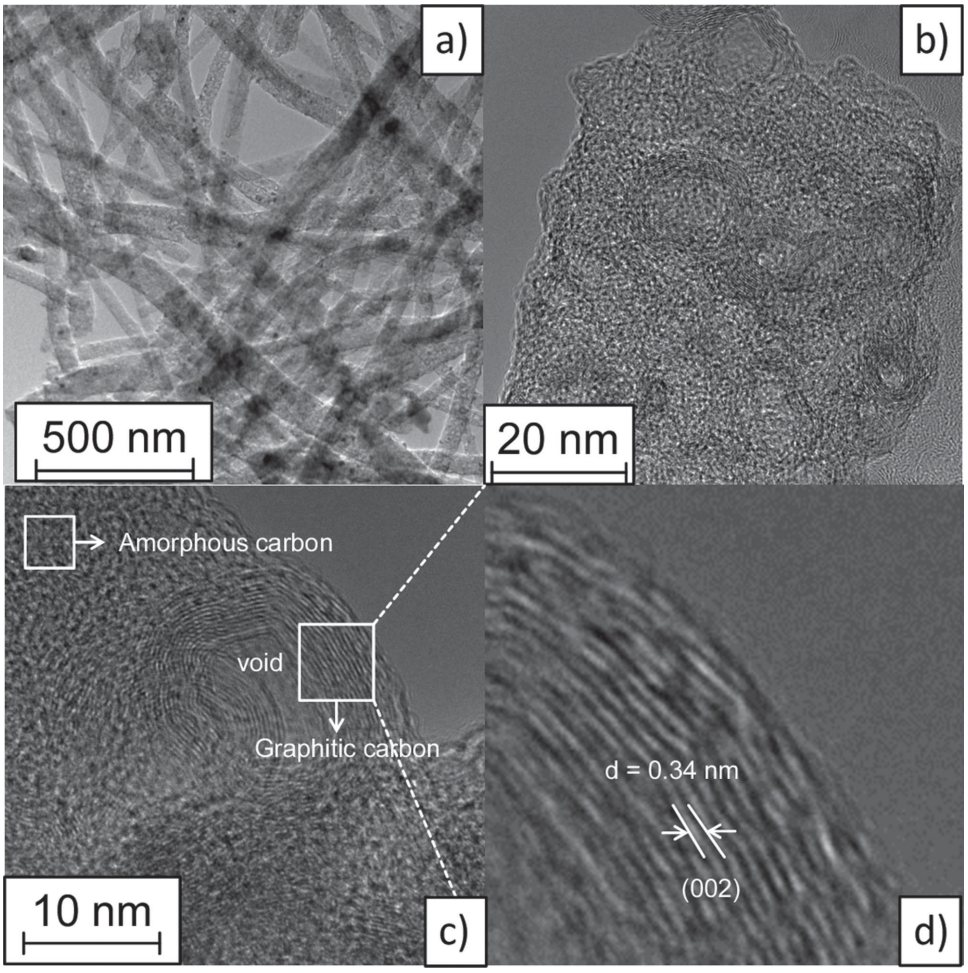

Figure 2. a) BF-TEM image of FS-ND ⊂ PGC-NW. b) HRTEM image of FS-ND ⊂ PGC-NW, indicating highly porous carbon nanowire. c) HRTEM images of selected area of FS-ND ⊂ PGC-NW, which shows coexistence of amorphous carbon, graphitic carbon, and void space within the carbon nanowires. d) Corresponding HRTEM image from marked region in c), clearly revealing lattice plane of graphitic carbon.

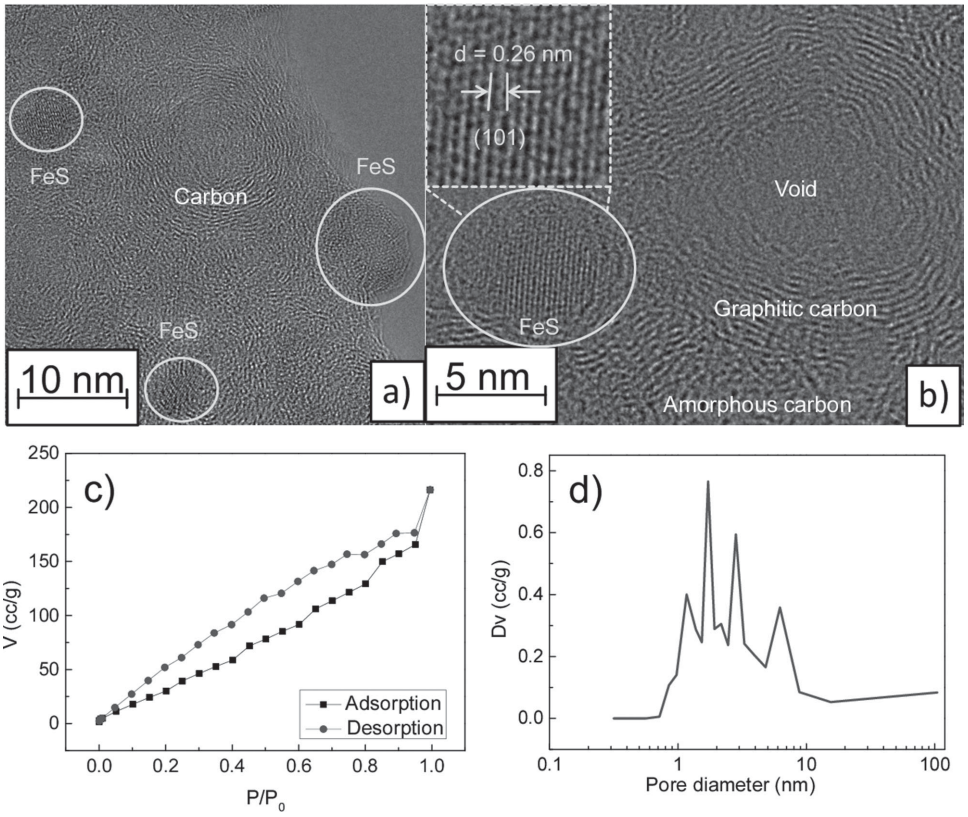

Figure 3. a) HRTEM images of selected and typical area of FS-ND ⊂ PGC-NW, which shows the distribution of FeS nanodots within the hollow tunneled graphitic carbon nanowire. b) HRTEM images of FS-ND ⊂ PGC-NW, which clearly shows the lattice plane of crystalline FeS and reveals coexistence and distribution of amorphous carbon, graphitic carbon, and void space within the carbon nanowires. c) Nitrogen adsorption/desorption isotherms of FS-ND ⊂ PGC-NW. d) The pore-size distribution plot calculated by the BLH method.

distribution of FeS nanodots within the amorphous/graphitic carbon nanowire is displayed in **Figure 3**a. As shown clearly, the mechanically isolated FeS nanodots are around 5–10 nm in diameter, and randomly distributed within the carbon nanowire. This confinement is highly beneficial for the conversion reaction, leading to better reversibility. The HRTEM image (Figure 3b) of FS-ND ⊂ PGC-NW displays clear lattice fringes with d-spacing of ≈0.26 nm, which is attributed to the (101) lattice plane of hexagonal FeS, indicating a high degree of crystallinity. Furthermore, as shown in Figure 3b, both size and shape of the FeS nanodots fit very well the void of graphitic carbon, in good agreement with the material evolution process we proposed above (Figure 1a). Surface area and pore structure of FS-ND ⊂ PGC-NW are further studied by nitrogen isothermal adsorption technique. As shown in Figure 3c, the result is a type IV isotherm with a hysteresis loop, indicating a nanoporous structure of high BET area (226 m^2 g^{-1}). The Barrett-Joyner-Halenda (BJH) pore-size distribution curve (Figure 3d) indicates that the pore sizes are in the range of 1–10 nm. Raman spectrum of FS-ND ⊂ PGC-NW is shown in Supporting Information, Figure S3. According to literature on Raman spectroscopy of carbon based materials, the D-band at ≈1360 cm^{-1} is attributed to structural disorder and imperfections, while the G-band at ≈1580 cm^{-1} is attributed to ordered graphite phase.[40] As suggested in the literature, the existence of the 2D-band (≈2700 cm^{-1}) and the low-intensity of the D-band when compared to the G-band (I_D/I_G = 0.96) indicate that the carbon is highly graphitized.[40–42]

In order to investigate the redox reactions taking place in FS-ND ⊂ PGC-NW, cyclic voltammetry (CV) was applied at a scanning rate of 0.1 mV s^{-1} for the Li/1 M $LiPF_6$ in ethylene carbonate (EC) - diethyl carbonate (DEC) /FS-ND ⊂ PGC-NW cell for the first five cycles (**Figure 4**a). In the first cycle, a single reduction peak was observed at ≈1.3 V, and one corresponding to oxidation appears at ≈1.8 V. These two peaks correspond to the redox behavior of conversion reaction of FeS ($FeS + 2Li^+ + 2e^- \rightarrow Fe + Li_2S$). While some researchers suggest that the conversion reaction occurs subsequently, according to[19]

$$2FeS + 2Li^+ + 2e^- \rightarrow Fe + Li_2FeS_2 \quad (1)$$

$$Li_2FeS_2 + 2Li^+ + 2e^- \rightarrow Fe + 2Li_2S \quad (2)$$

there is the other view point that the reactions (1) and (2) occur simultaneously owing to the relative slow diffusion of Li^+.[16] McMillan and co-workers proposed reduction of FeS to occur in a single-step since no intermediate Li_2FeS_2 was observed by ^{57}Fe Mössbauer spectroscopy.[15] From the second cycle onwards in the CV curves (Figure 4a), the reduction peaks are shifted to ≈1.4 V. The increased voltage after the

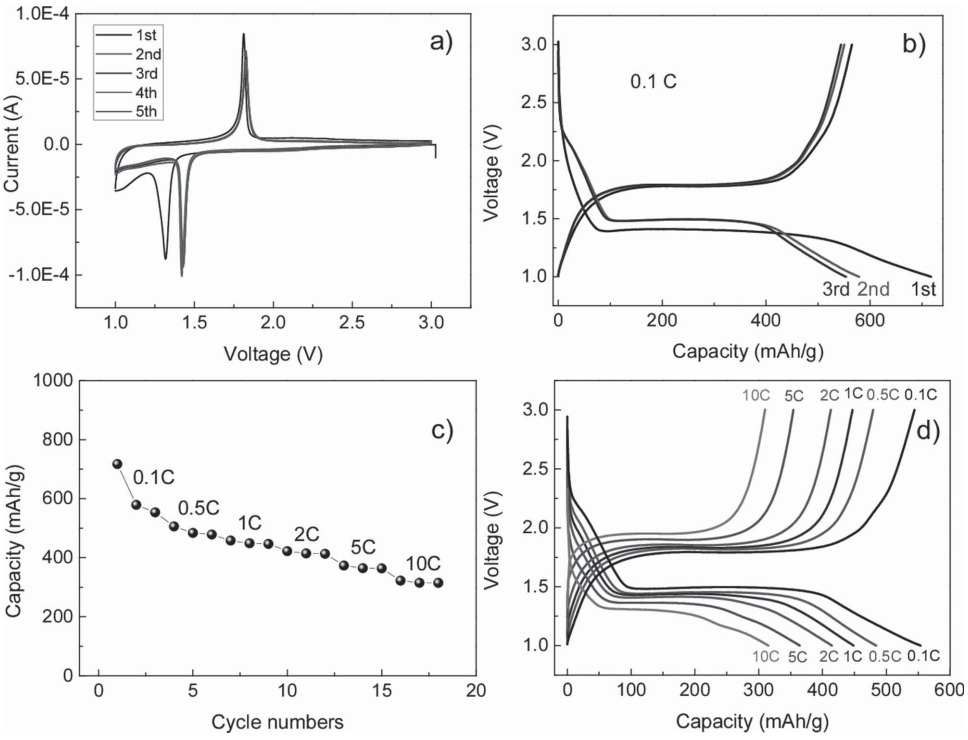

Figure 4. a) Cyclic voltammetry of FS-ND ⊂ PGC-NW for the first five cycles with scan rate of 0.1 mV s^{-1}. b) Charge and discharge profiles of FS-ND ⊂ PGC-NW for the first three cycles at 0.1 C rate. c) Rate performance of FS-ND ⊂ PGC-NW. d) Charge and discharge profiles of FS-ND ⊂ PGC-NW at different C rates.

initial lithiation is a widely reported phenomenon for many conversion electrodes,[43–46] which is mainly attributed to structure and stress/strain changes during the initial conversion process.[43,44] The oxidation peaks are still localized at ≈1.8 V. Almost overlapped CV curves from 3rd to 5th cycle indicate excellent reversibility.

The electrochemical performance of FS-ND ⊂ PGC-NW in terms of lithium storage is outstanding. Figure 4b displays the charge/discharge profiles for the first three cycles at 0.1 C in the voltage window of 1 V to 3 V. (Note that 1 C means that the full capacity can be discharged or charged in 1 h, corresponding to 609 mA g^{-1} in this work.) The first discharge plateau is around 1.4 V, and from the second one onwards, the discharge plateau increases to 1.5 V. The charge plateaus remain at ≈1.8 V. The capacity from the 2rd discharge cycle is 579 mA h g^{-1}, which corresponds to storing almost 2 Li per Fe ($FeS + 2Li^+ + 2e^- \rightarrow Fe + Li_2S$). Note that all the capacity values in this work refer to the mass of FeS. The carbon content of FS-ND ⊂ PGC-NW is not more than ≈31 wt%, as measured by elemental analysis (see the Experimental Section). As the FeS content in FS-ND ⊂ PGC-NW is around 70% by weight, the capacity data for the whole FS-ND ⊂ PGC-NW are pronouncedly good as well. The outstanding rate performance is demonstrated by the specific discharge capacities being around 579, 506, 458, 422, 373, 322 mA h g^{-1} at current rates of 0.1, 0.5, 1, 2, 5, 10 C, respectively (Figure 4c). Note that 10 C corresponds to as much as 6 A g^{-1}, which, in spite of the low voltage, gives rise to a rather high power output for this material. To the best of our knowledge, such a good rate performance of a FeS/Li cell in the voltage window of 1–3 V has not been reported before. The charge and discharge profiles for various C rates are displayed in Figure 4d. Surprisingly, well-defined, very flat and symmetric charge–discharge plateaus are observed. Although polarization becomes more obvious when the current densities increased from 0.1 C to 10 C, the charge and discharge plateaus are still clearly distinguishable.

Furthermore, FS-ND ⊂ PGC-NW exhibits a pronounced cycling stability. The specific discharge capacity is still as high as ≈400 mA h g^{-1} even after 50 cycles at 0.5 C with high Coulombic efficiencies as shown in **Figure 5**a. The Li-storage specific capacity of FS-ND ⊂ PGC-NW is distinctly higher than the commercially used intercalation cathode $LiCoO_2$ (≈140 mA h g^{-1}). Hence, as shown in Figure 5b, in spite of relatively lower voltage of FS-ND ⊂ PGC-NW, it still can deliver a higher discharge energy density when compared with $LiCoO_2$ (≈550 W h kg^{-1})[16], rendering FS-ND ⊂ PGC-NW a promising cathode for a room temperature lithium battery.

Using CV measurements we determine an effective diffusion coefficient based on Randles–Sevcik equation. Such an analysis is typically difficult for conversion reactions owing to the lack of well defined peaks in CV curves. Here, though, very distinguished peaks in CV curves are recorded at various scan rates (Figure 5c). Taking the geometric electrode area value, apparent diffusion coefficients of 5×10^{-14} cm^2 s^{-1} and 7×10^{-14} cm^2 s^{-1} are obtained for reduction and oxidation processes respectively (Supporting Information, Figure S1), which is in the similar range as the apparent diffusion coefficient obtained by the same method for $LiCoO_2$.[47]

Let us emphasize again the remarkable features of FS-ND ⊂ PGC-NW with respect to reversibility and polarization.

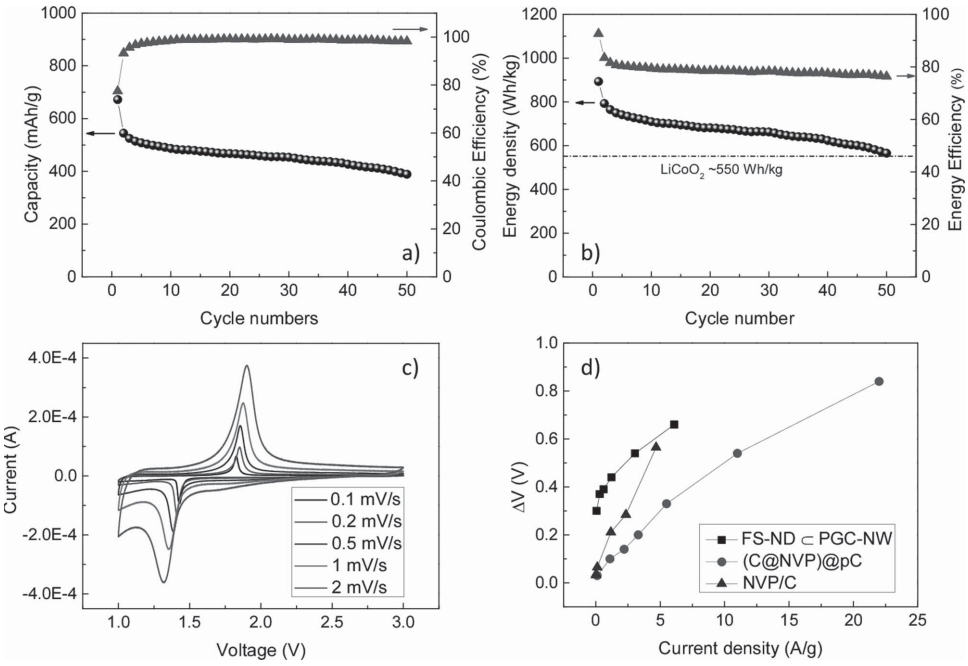

Figure 5. a) Cycling performance and Coulombic efficiency of FS-ND ⊂ PGC-NW at 0.5 C rate. b) Discharge energy density and energy efficiency of FS-ND ⊂ PGC-NW vs cycle number. c) Cyclic voltammetry curves of FS-ND ⊂ PGC-NW for various scan rate. d) ΔV-values of FS-ND ⊂ PGC-NW at different current densities in comparison with $Na_3V_2(PO_4)_3$/C based on phase transition instead of conversion reaction. ((C@NVP)@pC and NVP/C correspond to refs. [48] and [49].)

i) Reversibility: From the charge–discharge profiles (Figure 4b), well-defined, flat, symmetric charge, and discharge plateaus are observed, which is quite rare for conversion reaction of oxides or fluorides. The flat charge–discharge plateaus are rather similar to $LiFePO_4$[32] or the sodium battery cathode $Na_3V_2(PO_4)_3$,[48] where they are based on phase transition instead of phase decomposition. In fact, the plateau is also expected for a multiphase equilibrium in a nonvariant situation but its realization requires excellent kinetics, as they are observed here. The symmetric charge and discharge plateaus underscore the high reversibility for FS-ND ⊂ PGC-NW. We believe that the pre-confinement of the FeS nanodots in the porous graphitic carbon nanowires is crucial for this phenomenon, leading to an almost nucleation-free and diffusion-less conversion reaction.[31] ii) Polarization: Unsurprisingly, as shown in Supporting Information, Figure S2, owing to polarization, the discharge voltage is lower and the charge voltage is higher than the open circuit voltage (OCV) -value, expected from bulk thermodynamics. Typically, for conversion reactions, the polarization is extremely large especially for the initial discharge process (normally larger than 0.5 V). The observed asymmetry in the polarization behavior in Supporting Information, Figure S2 is at least to a great deal apparent, as based on too high an equilibrium voltage. Rather, for both an experimental as well as a thermodynamic point of view, the voltages of the conversion reaction are always different from the electromotive force (emf) calculated by the thermodynamic data.[11,31] According to our previous report,[31] the correction can be assessed by the change in the surface free energy $\Delta(2\gamma V/r)$ (γ: surface tension; V: molar value; r: radius of particle size; Δ denotes the change during the respective reaction). By roughly assuming equal values of γ and r values for Li_2S, Fe, and FeS, and neglecting the second term for macroscopic Li, the equilibrium cell voltage will be lowered by $[2\gamma/r(V_{Li_2S} + V_{Fe} - V_{FeS})]/2F$. If we assume γ of $\approx$1 J m^{-2} and r of 2 nm, and take V_{Li2S}, V_{Fe}, and V_{FeS} are 27.67, 7.09, and 18.16 cm^3 mol^{-1}, respectively, the real equilibrium emf is estimated to be lowered by around 90 mV, leading to a corrected emf of around 1.6 V. This then leads to a rather symmetrical polarization behavior. More importantly, for FS-ND ⊂ PGC-NW, as shown in Supporting Information, Figure S2, this polarization is distinctly smaller than in usual conversion reactions (typically at least 0.5 V). Here the initial discharge polarization is as small as 0.25 V, and after the first cycle the discharge polarization is even reduced to almost 0.15 V. The charge polarization is similarly small. Note that while this partitioning depends on the knowledge of the magnitude of the surface tensions, the total voltage loss in a cycle is naturally invariant. With the exception of the first cycle, it is as small as 300 mV, indicating also the absence of severe strain and interface resistances. Such a small voltage loss is quite impressive when compared to oxides, fluorides, or even other sulfides. Altogether, FS-ND ⊂ PGC-NW seems at the moment the best candidate for conversion storage amongst all the transition metal compounds.

Since very flat and symmetric charge and discharge plateaus are observed for FS-ND ⊂ PGC-NW, the polarization can be investigated as a function of current density (ΔV–I plot) enabling a deeper understanding. As the (dis)charge profiles of FS-ND ⊂ PGC-NW show similarity with the extremely well-performing $Na_3V_2(PO_4)_3$, which is based on phase transition, we compare ΔV–I plots of FeS and $Na_3V_2(PO_4)_3$ (Figure 5d, Supporting Information, Table S1). As shown in Figure 5d,

due to the intrinsic large voltage hysteresis behavior for conversion reaction, the ΔV value of FS-ND ⊂ PGC-NW is higher than that of $Na_3V_2(PO_4)_3$ at small current density, but the slope of the ΔV-I plot for FS-ND ⊂ PGC-NW (black curve) is smaller than that of the $Na_3V_2(PO_4)_3$/C composite[49] (blue curve), and rather comparable to the carbon-coated $Na_3V_2(PO_4)_3$ embedded in porous carbon matrix (((nano-0D $Na_3V_2(PO_4)_3$)⊂ (nano-0D carbon)) ⊂ (porous-carbon))[34] (red curve), which was found to outperform Li-cathodes at high rates.[48]

The excellent electrochemical performance as well as impressive conversion chemistry of FS-ND ⊂ PGC-NW can be attributed to its unique morphology: 1) Small mechanically isolated but electrochemically well connected FeS nanodots are fabricated. This not only excludes or at least mitigates nucleation and diffusion problems inherent to usual conversion reactions, but also effectively accommodates the volume change and prevents the aggregation of particles during charge–discharge process, leading to good reversibility and cycling stability. 2) The small dimensions of FeS nanodots are helpful for the internal Li-transport, too. 3) The graphitic carbon nanowires easily percolate and enable fast electron transport (compared to amorphous carbon nanowires) to the electroactive particles; while fast ion transport is guaranteed by the network and the small nanowire diameter. 4) The nanopores in the graphitic nanowires are not only beneficial for the electrolyte penetration but also buffer the particles expansion-shrinkage during cycling. Furthermore the fibers act as binder and particle holders. In addition, Ostwald ripening is suppressed owing to suppressed Fe-ion transport between FeS particles.

3. Conclusions

In summary, for the first time, by using electrospinning technique followed by biomolecular (L-cysteine)-assisted hydrothermal method, FeS nanodots (≈5–10 nm) encapsulated in highly porous (226 m^2 g^{-1}) graphitic carbon nanowires (≈100 nm) are successfully prepared. Such nanodots show excellent storage performance. Owing to the voltage regime they can be used as anodes or cathodes. Here we stress their usability as powerful cathode materials, as the comparatively low cell voltage may be more than compensated by the large capacities and the low polarization. We observe specific capacities in the range of 300–600 mA h g^{-1} if current rates are varied in the range of 0.1 C to 10 C, highlighting the excellent rate capability for a room temperature rechargeable FeS/Li cells with liquid electrolyte ($LiPF_6$ in EC/DEC) in the voltage window of 1–3V. The energy density of FS-ND ⊂ PGC-NW is even higher than that of the commercial lithium cathode ($LiCoO_2$). In terms of conversion chemistry, well-defined, flat, and symmetric charge–discharge plateaus indicate a remarkable reversibility, which is also exhibited by the cycling stability. The initial discharge polarization is as small as 0.25 V, and further reduces to 0.15 V after the first cycle. The total voltage loss in a cycle is less than 0.3 V, which is very impressive for conversion electrodes. We hope that the current work helps paving the way for developing earth abundant, environmental friendly, and low cost FeS cathodes based on conversion reaction.

4. Experimental Section

Synthesis: $Fe(NO_3)_3{\cdot}9H_2O$ (0.4 M) was dissolved in water ethanol mixture (1:1 volume ratio) and polyvinylpyrrolidone (PVP, M_v = 1 300 000 g mol^{-1}) (8 wt%) was added in the solution to form viscous solution. The resultant precursor solution was poured into a syringe connected to a 1.6 mm diameter metal needle. The flow rate was ≈10 μL min^{-1} and a grounded stainless steel was placed 15 cm below the spinneret to collect the nanowires. A 20 kV high voltage was applied by a high voltage power supply (Model HCE35–35000, FUG DC power source, Germany). The as-collected electrospun fibers were calcined in a tube furnace at 750 °C for 2 h with 2 °C min^{-1} heating rate. The obtained powder together with L-Cysteine and glucose (with the weight ratio of 1:10:1) were placed into a 50 mL Teflon-lined autoclave by hydrothermal treated at 190 °C for 24 h. After washed by water 3 times, the collected powder was finally annealed in Ar at 700 °C for 2 h with heating rate of 5 °C min^{-1}.

Structural and Electrochemical Characterization: XRD measurements were done with a Philips PW 3020 diffractometer using Cu-Kα radiation. SEM was carried out using a JEOL 6300F field-emission scanning electron microscopy (JEOL, Tokyo, Japan) operated at 15 kV. HRTEM was performed by a JEOL 4000FX transmission electron microscope (JEOL, Tokyo, Japan) operated at 400 kV. The carbon content is measured by carbon sulfur determinator (ELTRA, CS800), through combustion of the material in a stream of oxygen to form CO_2 which is detected by IR-spectroscopy. Raman spectrum is measured by Labram V010 with a 532 nm diode laser. FS-ND ⊂ PGC-NW (70 wt%), carbon black (20 wt%, Super-P, Timcal), and poly(vinylidene fluoride) binder (10 wt%, Aldrich) in N-methylpyrrolidone were mixed to form a homogeneous slurry. The obtained slurry was pasted on Cu current collector, followed by drying in a vacuum oven for 12 hours at 80 °C. Electrochemical test cells (Swagelok-type) were assembled in an argon-filled glove box (O_2 ≤ 0.1 ppm, H_2O ≤ 3 ppm) with the coated Cu disk as working electrode, lithium metal foil as the counter/reference electrode, and 1 M solution of $LiPF_6$ in a 1:1 vol/vol mixture of ethylene carbonate (EC) and diethyl carbonate (DEC) as the electrolyte. Glass fiber (Whatman) was used as separator. The batteries were discharged and charged galvanostatically in the fixed voltage window between 1 and 3 V on an Arbin MSTAT battery tester at room temperature. Cyclic voltammetry was measured by Voltalab 80 electrochemical workstation at various scan rates.

Supporting Information

Supporting Information is available from the Wiley Online Library or from the author.

Acknowledgements

We would like to thank Peter Kopold for TEM and HRTEM tests, Anette Fuchs for SEM and BET measurements, Helga Hoier for XRD, and Armin Schulz for Raman tests. This work was financially supported by the Sofja Kovalevskaja award of the Alexander von Humboldt Foundation, the National Natural Science Foundation of China (Grant Nos. 21171015 and 21373195), the Recruitment Program of Global Experts, the New Century Excellent Talents in University (NCET), the Fundamental Research Funds for the Central Universities (WK2060140014, WK2060140016), the Collaborative Innovation Center of Suzhou Nano Science and Technology, the Max-Planck Society, as well as the European Union Seventh Framework Programme (FP7/2007–2013) under Grant Agreement No. 312483 (ESTEEM2).

Received: December 17, 2014
Revised: January 23, 2015
Published online: March 2, 2015

[1] B. Dunn, H. Kamath, J.-M. Tarascon, *Science* **2011**, *334*, 928.
[2] J. M. Tarascon, M. Armand, *Nature* **2001**, *414*, 359.
[3] P. Poizot, S. Laruelle, S. Grugeon, L. Dupont, J. M. Tarascon, *Nature* **2000**, *407*, 496.
[4] P. Balaya, H. Li, L. Kienle, J. Maier, *Adv. Funct. Mater.* **2003**, *13*, 621.
[5] H. Li, P. Balaya, J. Maier, *J. Electrochem. Soc.* **2004**, *151*, A1878.
[6] B. Wang, J. S. Chen, H. B. Wu, Z. Wang, X. W. Lou, *J. Am. Chem. Soc.* **2011**, *133*, 17146.
[7] H. Hwang, H. Kim, J. Cho, *Nano Lett.* **2011**, *11*, 4826.
[8] X. Zhou, L.-J. Wan, Y.-G. Guo, *Chem. Commun.* **2013**, *49*, 1838.
[9] C. Li, L. Gu, S. Tsukimoto, P. A. van Aken, J. Maier, *Adv. Mater.* **2010**, *22*, 3650.
[10] J. Cabana, L. Monconduit, D. Larcher, M. R. Palacín, *Adv. Mater.* **2010**, *22*, E170.
[11] J. Maier, *Angew. Chem. Int. Ed.* **2013**, *52*, 4998.
[12] Z. Tomczuk, B. Tani, N. C. Otto, M. F. Roche, D. R. Vissers, *J. Electrochem. Soc.* **1982**, *129*, 925.
[13] D. Bernardi, J. Newman, *J. Electrochem. Soc.* **1987**, *134*, 1309.
[14] J. Lesinski, J. Izydorek, L. Werblan, *J. Power Sources* **1989**, *27*, 337.
[15] C. H. W. Jones, P. E. Kovacs, R. D. Sharma, R. S. McMillan, *J. Phys. Chem.* **1990**, *94*, 4325.
[16] J. Liu, Y. Wen, Y. Wang, P. A. van Aken, J. Maier, Y. Yu, *Adv. Mater.* **2014**, *26*, 6025.
[17] S.-B. Son, T. A. Yersak, D. M. Piper, S. C. Kim, C. S. Kang, J. S. Cho, S.-S. Suh, Y.-U. Kim, K. H. Oh, S.-H. Lee, *Adv. Energy Mater.* **2014**, *4*,1300961.
[18] T. A. Yersak, C. Stoldt, S.-H. Lee, *J. Electrochem. Soc.* **2013**, *160*, A1009.
[19] S.-H. Kim, Y.-J. Choi, D.-H. Kim, S.-H. Jung, K.-W. Kim, H.-J. Ahn, J.-H. Ahn, H.-B. Gu, *Surf. Rev. Lett.* **2008**, *15*, 35.
[20] N.-S. Choi, Z. Chen, S. A. Freunberger, X. Ji, Y.-K. Sun, K. Amine, G. Yushin, L. F. Nazar, J. Cho, P. G. Bruce, *Angew. Chem. Int. Ed.* **2012**, *51*, 9994.
[21] T. D. Kaun, P. A. Nelson, L. Redey, D. R. Vissers, G. L. Henriksen, *Electrochim. Acta* **1993**, *38*, 1269.
[22] Y. Shao-Horn, S. Osmialowski, Q. C. Horn, *J. Electrochem. Soc.* **2002**, *149*, A1499.
[23] X. Wang, Q. Xiang, B. Liu, L. Wang, T. Luo, D. Chen, G. Shen, *Sci. Rep.* **2013**, *3,* 2007.
[24] C. Xu, Y. Zeng, X. Rui, N. Xiao, J. Zhu, W. Zhang, J. Chen, W. Liu, H. Tan, H. H. Hng, Q. Yan, *ACS Nano* **2012**, *6*, 4713.
[25] T. A. Yersak, H. A. Macpherson, S. C. Kim, V.-D. Le, C. S. Kang, S.-B. Son, Y.-H. Kim, J. E. Trevey, K. H. Oh, C. Stoldt, S.-H. Lee, *Adv. Energy Mater.* **2013**, *3*, 120.
[26] K. Takada, Y. Kitami, T. Inada, A. Kajiyama, M. Kouguchi, S. Kondo, M. Watanabe, M. Tabuchi, *J. Electrochem. Soc.* **2001**, *148*, A1085.
[27] L. Zhao, X. Yu, J. Yu, Y. Zhou, S. N. Ehrlich, Y.-S. Hu, D. Su, H. Li, X.-Q. Yang, L. Chen, *Adv. Funct. Mater.* **2014**, *24*, 5557.
[28] C. Dong, X. Zheng, B. Huang, M. Lu, *Appl. Surf. Sci.* **2013**, *265*, 114.
[29] B.-C. Kim, K. Takada, N. Ohta, Y. Seino, L. Zhang, H. Wada, T. Sasaki, *Solid State Ionics* **2005**, *176*, 2383.
[30] L. Fei, Q. Lin, B. Yuan, G. Chen, P. Xie, Y. Li, Y. Xu, S. Deng, S. Smirnov, H. Luo, *ACS Appl. Mater. Interfaces* **2013**, *5*, 5330.
[31] C. Zhu, X. Mu, P. A. van Aken, Y. Yu, J. Maier, *Angew. Chem. Int. Ed.* **2014**, *53*, 2152.
[32] C. Zhu, Y. Yu, L. Gu, K. Weichert, J. Maier, *Angew. Chem. Int. Ed.* **2011**, *50*, 6278.
[33] X. Zhou, Z. Dai, S. Liu, J. Bao, Y.-G. Guo, *Adv. Mater.* **2014**, *26*, 3943.
[34] J. Maier, *Faraday Discuss.* **2014**, DOI: 10.1039/C4FD00135D.
[35] C. Zhang, J. Li, C. Shi, C. He, E. Liu, N. Zhao, *J. Energy Chem.* **2014**, *23*, 324.
[36] K. Chang, W.-X. Chen, H. Li, H. Li, *Electrochim. Acta* **2011**, *56*, 2856.
[37] J. Pan, S. Xiong, B. Xi, J. Li, J. Li, H. Zhou, Y. Qian, *Eur. J. Inorg. Chem.* **2009**, *2009*, 5302.
[38] Q. Wang, R. Gao, J. Li, *Appl. Phys. Lett.* **2007**, *90*, 143107.
[39] B. Zhang, X. C. Ye, W. Dai, W. Y. Hou, Y. Xie, *Chem. Eur. J.* **2006**, *12*, 2337.
[40] Y. Chen, Z. Lu, L. Zhou, Y.-W. Mai, H. Huang, *Nanoscale* **2012**, *4*, 6800.
[41] N. Liu, K. Kim, P.-C. Hsu, A. N. Sokolov, F. L. Yap, H. Yuan, Y. Xie, H. Yan, Y. Cui, H. Y. Hwang, Z. Bao, *J. Am. Chem. Soc.* **2014**, *136*, 17284.
[42] Y. Aykut, *ACS Appl. Mater. Interfaces* **2012**, *4*, 3405.
[43] F. Ma, A. Yuan, J. Xu, *ACS Appl. Mater. Interfaces* **2014**, *6*, 18129.
[44] J. Guo, Q. Liu, C. Wang, M. R. Zachariah, *Adv. Funct. Mater.* **2012**, *22*, 803.
[45] F. Wang, R. Robert, N. A. Chernova, N. Pereira, F. Omenya, F. Badway, X. Hua, M. Ruotolo, R. Zhang, L. Wu, V. Volkov, D. Su, B. Key, M. S. Whittingharn, C. P. Grey, G. G. Amatucci, Y. Zhu, J. Graetz, *J. Am. Chem. Soc.* **2011**, *133*, 18828.
[46] X. Q. Yu, Y. He, J. P. Sun, K. Tang, H. Li, L. Q. Chen, X. J. Huang, *Electrochem. Commun.* **2009**, *11*, 791.
[47] Y. H. Rho, K. Kanamura, *J. Electrochem. Soc.* **2004**, *151*, A1406.
[48] C. Zhu, K. Song, P. A. van Aken, J. Maier, Y. Yu, *Nano Lett.* **2014**, *14*, 2175.
[49] K. Saravanan, C. W. Mason, A. Rudola, K. H. Wong, P. Balaya, *Adv. Energy Mater.* **2013**, *3*, 444.